ACS Catalysis

pubs.acs.org/acscatalysis

Research Article

Finding Key Factors for Efficient Water and Methanol Activation at Metals, Oxides, MXenes, and Metal/Oxide Interfaces

Hai-Yan Su, Keju Sun,* Xiang-Kui Gu, Sha-Sha Wang, Jing Zhu, Wei-Xue Li, Chenghua Sun, and Federico Calle-Vallejo*

Cite This: *ACS Catal.* 2022, 12, 1237−1246

Read Online

ACCESS | Metrics & More | Article Recommendations | Supporting Information

ABSTRACT: Activating water and methanol is crucial in numerous catalytic, electrocatalytic, and photocatalytic reactions. Despite extensive research, the optimal active sites for water/methanol activation are yet to be unequivocally elucidated. Here, we combine transition-state searches and electronic charge analyses on various structurally different materials to identify two features of favorable O−H bond cleavage in H_2O, CH_3OH, and hydroxyl: (1) low barriers appear when the charge of H moieties remains approximately constant during the dissociation process, as observed on metal oxides, MXenes, and metal/oxide interfaces. Such favorable kinetics is closely related to adsorbate/substrate hydrogen bonding and is enhanced by nearly linear O−H−O angles and short O−H distances. (2) Fast dissociation is observed when the rotation of O−H bonds is facile, which is favored by weak adsorbate binding and effective orbital overlap. Interestingly, we find that the two features are energetically proportional. Finally, we find conspicuous differences between H_2O/CH_3OH and OH activation, which hints toward the use of carefully engineered interfaces.

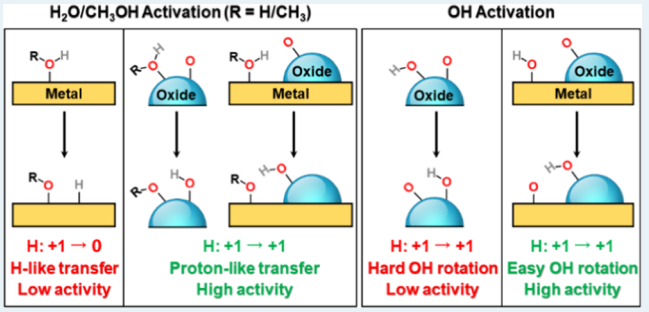

KEYWORDS: *H_2O dissociation, CH_3OH dissociation, oxides, metal/oxide interfaces, proton-like hydrogen transfer, O−H bond rotation, DFT calculations*

1. INTRODUCTION

Water plays a crucial role in numerous catalytic reactions. It can either act as a reactant for surface reactions such as the water−gas shift and methane/methanol steam reforming or facilitate reactions as moisture in the reactant gases.[1−8] In addition, it is used as a solvent in countless inorganic and organic reactions and is also important in electrochemistry, fuel cells, and corrosion science and technology.[9,10] Furthermore, apart from being a commodity chemical, methanol has attracted great interest in recent years for hydrogen production via methanol steam reforming, the development of direct methanol fuel cells to be used in small portable devices, and the potential of CH_3OH photocatalytic oxidation.[2,11−15] In view of their high thermodynamic stability, the activation of water or methanol is habitually a decisive part of catalytic pathways, often the rate-limiting step.[1,2,13,16−20]

Although numerous studies have been devoted to identifying the active sites for water and methanol activation, they are still a matter of debate in view of the coexistence of numerous structural motifs at catalytic surfaces. For instance, some authors have suggested that oxide supports (e.g., TiO_{2-x}, CeO_{2-x}) are responsible for water activation in the water−gas shift.[16,21−23] Others have shown that both metals and oxide supports at metal/oxide interfaces (e.g., Cu/FeO_x, Ni/TiO_{2-x}, Au/TiO_{2-x}) directly participate in water activation.[24−26] Moreover, some authors claim that metals (Cu) or metal cations ($Pt^{\delta+}$, $Au^{\delta+}$) are the active sites for the water−gas shift.[27−29] In addition, discrepancies exist about methanol activation on CuZn alloy sites or Cu/ZnO interfaces at Cu/ZnO catalysts during catalytic methanol steam reforming.[30−35] These conflicting views greatly hamper the design and implementation of improved catalysts and call for fundamental studies that outline the different interactions between H_2O/CH_3OH and various structural motifs/sites. In this context, the challenge lies in identifying the common features of swift activation kinetics among structurally different materials.

In this study, we identify two such features among metals, oxides, MXenes, and metal/oxide interfaces combining the climbing-image nudged elastic band (CI-NEB) method[36] for the location of transition states (TSs) and the Bader charge analysis.[37] Specifically, Cu(111), Co(0001), Pt(111), rutile

Received: July 29, 2021
Revised: December 24, 2021

https://doi.org/10.1021/acscatal.1c03405
ACS Catal. 2022, 12, 1237−1246

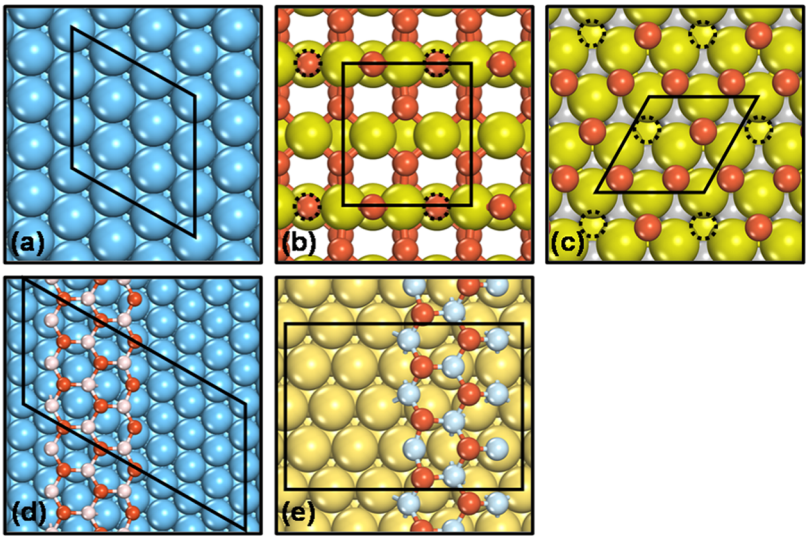

Figure 1. Top view of (a) Cu(111), (b) TiO_2(110), (c) $Ti_3C_2O_2$(0001), (d) Cu/ZnO, and (e) Pt/FeO. Blue, olive, pink, yellow, light blue, and red balls and black dashed circles represent Cu, Ti, Zn, Pt, Fe, and O atoms and O vacancies, respectively.

TiO_2(110), and $Ti_3C_2O_2$(0001), together with Pt/FeO and Cu/ZnO interfaces are used to model various structural motifs/sites in view of their superior performance in relevant applications, such as water−gas shift, methanol steam reforming, and CH_3OH photocatalytic oxidation.[1,2,15]

The first feature refers to the charge state of H moieties, as there are clear energetic differences between H-like transfer and proton-like transfer during H_2O, OH, and CH_3OH activation. O−H bond scission in H_2O and CH_3OH on metals occurs via a H-like transfer process with large associated energy barriers. Conversely, such cleavage on oxides, MXenes, and metal/oxide interfaces occurs via a proton-like transfer with small barriers. The second feature refers to O−H bond rotation. Weak binding and effective orbital overlap between O atoms in OH and substrates are found to facilitate O−H bond rotation and dissociation. Finally, we show that although H_2O, CH_3OH, and OH interactions with metals, oxides, MXenes, and metal/oxide interfaces are fundamentally different, the two aforementioned features are energetically proportional.

2. METHODS

Spin-unrestricted density functional theory (DFT) calculations were performed with the Vienna Ab initio Simulation Package (VASP).[38] The interaction between ionic cores and valence electrons was described by the projector-augmented wave (PAW) method,[39] and the Kohn−Sham valence electronic wavefunction was expanded using a plane-wave basis set with a kinetic energy cutoff of 400 eV. Exchange−correlation effects on the total energies were calculated within the generalized gradient approximation (GGA) using the Perdew−Burke−Ernzerhof (PBE) exchange−correlation functionals.[40] Section S9 in the Supporting Information (SI) shows that the effect of D3 dispersion corrections on the adsorption energies is mostly a constant downward shift with a minor effect on the trends.[41] The total energies were converged to within 10^{-4} eV, and the forces on the atoms were converged to within 0.05 eV/Å. The lattice constants for bulk Cu (face-centered cubic (fcc)), Co (hexagonal close-packed (hcp)), Pt (fcc), TiO_2 (rutile), and the $Ti_3C_2O_2$ (MXene) were calculated to be 3.64, 2.50/4.03, 3.99, 4.67/2.97, and 3.04 Å, in line with the experimental values of 3.62, 2.51/4.06, 3.92, 4.59/2.96, and 3.057 Å.[42,43]

Cu(111), Co(0001), and Pt(111) were modeled using four-layer slabs with (3 × 3) surface unit cells (Figure 1a). The surface Brillouin zones were sampled with (4 × 4 × 1) Monkhorst−Pack *k*-point grid meshes.[44] The two topmost layers and the adsorbates were fully relaxed, and the remaining layers were fixed at the converged bulk positions. (2 × 1) Four-layer and five-layer slabs were used to model TiO_2(110) and $Ti_3C_2O_2$(0001) surface; see Figure 1b,c. The two topmost layers of TiO_2(110) and all of the layers of $Ti_3C_2O_2$(0001) together with the adsorbates were relaxed. The Brillouin zones were sampled with (4 × 4 × 1) and (5 × 5 × 1) Monkhorst−Pack grids.[44] A one-layer graphite-like (3 × 3) ZnO(0001) ribbon, with an in-plane lattice of 3.30 Å, on a three-layer (4 × 8) Cu(111) slab was adopted to simulate the Cu/ZnO interface (Figure 1d). The Brillouin zone was sampled with a (1 × 2 × 1) Monkhorst−Pack grid. The two bottommost Cu layers and the four leftmost ZnO columns were frozen, while the remaining atoms in the metal slab and the oxide together with the adsorbates were relaxed. The Pt/FeO interface was modeled by a $(2\sqrt{3} \times 5)$ rectangular supercell, including a bilayer FeO ribbon with three columns of Fe atoms and two columns of O atoms on a three-layer Pt(111) slab, as shown in Figure 1e. A single *k*-point located at (0.25, −0.25, 0) was used to sample the surface Brillouin zone. The Pt layers and the three rightmost FeO columns were frozen, while the remaining atoms in the oxide were relaxed together with the adsorbates. The DFT + *U* approach was used to correct the on-site Coulomb repulsion of 3d electrons of Zn and Fe atoms in the Cu/ZnO and Pt/FeO interfaces, with *U*−*J* values of 4.7 and 3.0 eV, respectively.[45,46] A vacuum region of at least 15 Å sufficed to avoid interactions between periodically repeated slabs along the *z*-direction for all of the systems studied. More details about the models can be found in previous works.[47−49]

The adsorption energy (ΔE_{Ads}) was calculated using H_2O, CH_3OH, OH, and H_2 in the gas phase as reference states since they are reasonably well described within DFT.[50,51] A lower (more negative) ΔE_{Ads} implies stronger binding, while a higher (more positive) ΔE_{Ads} implies weaker binding. All transition states (TSs) were located by the CI-NEB method,[36] and saddle points were confirmed by vibrational frequency analysis. The relaxations stopped when the residual forces on each atom

https://doi.org/10.1021/acscatal.1c03405
ACS Catal. 2022, 12, 1237−1246

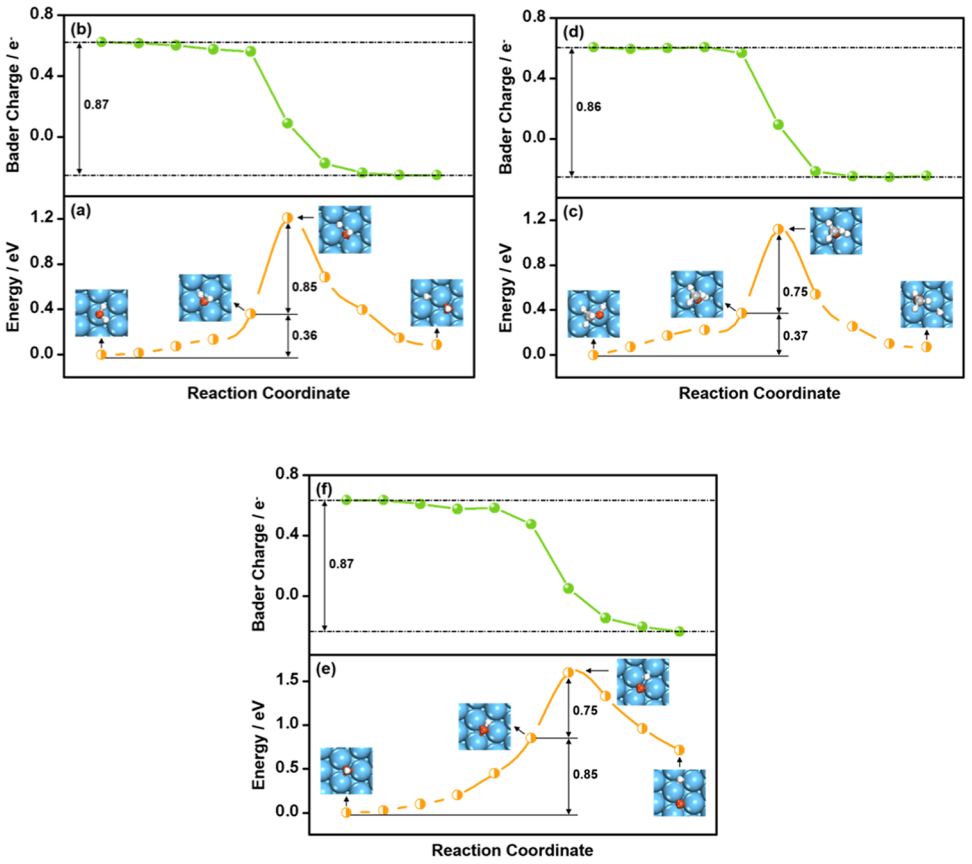

Figure 2. Energies and Bader charges on Cu(111) of a dissociating H moiety along the reaction coordinate for $*H_2O \rightarrow *OH + *H$ (a, b); $*CH_3OH \rightarrow *CH_3O + *H$ (c, d); and $*OH \rightarrow *O + *H$ (e, f). Insets: snapshots of the initial, preconditioning, transition, and final states.

were smaller than 0.05 eV/Å. The elementary activation barrier ($\Delta E_{Act} = E_{TS} - E_{IS}$, where TS and IS stand for transition and initial states, respectively) and reaction energy ($\Delta H = E_{FS} - E_{IS}$, where FS stands for final state) were calculated with respect to the co-adsorbed states of the species on the surfaces (for instance, $\Delta H_{H_2O} = E_{*H+*OH} - E_{*H_2O}$). We decompose the overall activation energy into two parts, namely, a preconditioning barrier and a dissociation barrier: $\Delta E_{Act} = \Delta E_1 + \Delta E_2$. We note that to univocally define the preconditioning state, the rotation of O−H bonds and their stretching need to be successive events. However, our CI-NEBs have no specific constraints along the reaction coordinate such that the end of a rotation coincides with the stretching of O−H bonds by no more than 0.09 Å for all of the molecules studied; see Δd_1 in Table S1. We evaluated the effect of such overlap between rotation and stretching on the energy of the preconditioning states ΔE_1 (see Tables S2 and S3 and more details in Section S1) and found that the small variation observed in O−H bond distances (<0.09 Å) from the initial states to the preconditioning states does not change the main conclusions of the present analysis (Figure S1). Compared to Δd_1, the variation in the dissociating O−H bond distance between transition states and preconditioning steps (Δd_2) is significantly larger, falling in the range of 0.04−0.71 Å (Table S1). We also define the rotation angle (∠ABC) of the dissociating O−H bond from the initial to the preconditioning step in Figure S2 and Table S4 to better describe the rotation of O−H bonds.

The Bader charge analysis was performed using a grid-based weight method[37] in which the expression for the fraction of space neighboring each grid point that flows to its neighbors is used as a weight for the discrete integration of functions over the Bader volume. In this context, a positive or negative charge means charge depletion or charge accumulation, respectively.

3. RESULTS AND DISCUSSION

3.1. H_2O, CH_3OH, and OH Activation on Metal Surfaces. H_2O binds weakly through O (Figures 2a, S3a, and S4a) at atop sites, with a flat-lying geometry (O and H at nearly identical heights above the surface), on metal surfaces. The calculated ΔE_{Ads} are −0.17, −0.28, and −0.24 eV on Cu(111), Co(0001), and Pt(111), respectively, as listed in Table S5. Such atop sites have been experimentally identified at low coverage and low temperature (<20 K) by scanning tunneling microscopy on Pt(111)[52] and Cu(110),[53] and predicted with DFT calculations to be the most stable adsorption sites on a number of close-packed and open metal surfaces.[54,55] This is because the dipole moment of H_2O molecules at these sites is aligned almost parallel to the surface plane, which favors the interaction of the $1b_1$ molecular orbital of H_2O with the surface bands.[56]

Taking adsorbed H_2O as the initial state (IS), we studied its dissociation on Cu(111), Co(0001), and Pt(111); see Table S6 and Figures 2a, S3a, and S4a. According to Table S6, the activation energies (ΔE_{Act}) fall in the range of 0.88−1.21 eV, in agreement with previous DFT studies.[19,57−59] These results indicate that H_2O dissociation is difficult on metal surfaces at low temperatures. To rationalize these results, we analyzed how the energies and Bader charges of the dissociating H moiety change along the reaction coordinate on Cu(111).

https://doi.org/10.1021/acscatal.1c03405
ACS Catal. 2022, 12, 1237−1246

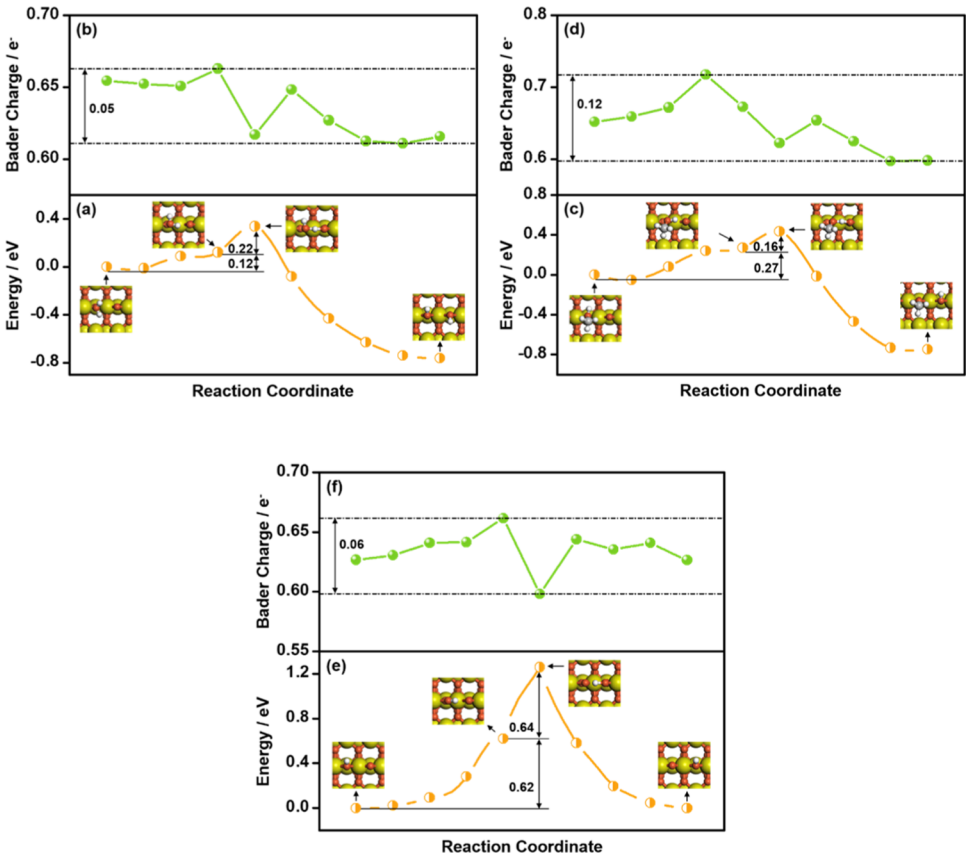

Figure 3. Energies and Bader charges on TiO_2(110) of a dissociating H moiety along the reaction coordinate for $*H_2O \rightarrow *OH + *H$ (a, b); $*CH_3OH \rightarrow *CH_3O + *H$ (c, d); and $*OH + *O \rightarrow *O + *OH$ (e, f). Insets: snapshots of the initial, preconditioning, transition, and final states.

The process begins with O moving from the top site to the hcp site and a rotation of the O−H bond. The rotation angles (∠ABC) of the dissociating O−H bond from the initial to the preconditioning state can be found in Figure S2 and Table S4. As a result, the water molecule is closer to the surface (generally by about 0.45 Å) with respect to the IS, and the O and H atoms differ in height above the surface. As shown in Table S1 and Figure 2a,b, the movement and rotation do not cause large variations of the O−H bond lengths (0.03 Å), energies (0.36 eV), and Bader charges of the dissociating H moiety (0.06 e^-). However, as the H−OH distance increases to 1.44 Å at the TS, the H moiety breaks its bond with O in H_2O and moves to an adjacent fcc site on Cu(111), with a net energy increase of 0.85 eV. Figure 2b shows that H exists in the form of a proton in adsorbed H_2O, with a Bader charge of 0.62−0.56 e^-. It becomes atomic H (0.09 to −0.25 e^-) on Cu(111) after the O−H bond is broken. This suggests that H_2O dissociation on Cu(111) is a H-like transfer process, where the H moiety in H_2O needs 0.53 e^- (from 0.62 to 0.09 e^-) to yield a H atom at the TS during dissociation, which entails a significant energy cost. This analysis also holds for Co(0001) and Pt(111), and explains the high activation energies (ΔE_{Act}) for H_2O dissociation on metals; see Figures S3 and S4.

CH_3OH adsorption and activation are similar to those of H_2O on metals. Briefly, CH_3OH also binds through O in an atop configuration (Figures 2c, S3c, and S4c), with ΔE_{Ads} comparable to H_2O on Cu(111), Co(0001), and Pt(111), as listed in Table S5. O−H bond scission in CH_3OH has a high ΔE_{Act} of 0.75−1.12 eV on metals (Table S6), implying that CH_3OH dissociation is as difficult as H_2O dissociation. As shown in Figure 2c, the reaction coordinate on Cu(111) proceeds through an initial O diffusion from the top site to the hcp site, accompanied by a rotation of the O−H and C−O bonds (Table S4). CH_3OH moves closer to the surface (generally by about 0.61 Å) during the surface diffusion and rotation, with a small change in the O−H bond lengths (0.02 Å), energies (0.37 eV), and Bader charges of the dissociating H (0.04 e^-); see Table S1 and Figure 2c,d. After that, the O−H distance increases appreciably (by 0.43 Å), and so does the energy (by 0.75 eV) until the TS is reached. At the TS, the O−H bond is broken with H now bound to Cu, and the Bader charge of the dissociating H is lowered by as much as 0.52 e^- relative to the IS. Therefore, similar to H_2O dissociation, CH_3OH dissociation on metal surfaces is a H-like transfer process requiring significant charge transfer and energy expenses.

Moreover, the reaction coordinate of OH dissociation on Cu(111) is composed of a rotation of the O−H bond from an almost perpendicular configuration to one that is parallel to the surface plane (Figure S2 and Table S4), followed by its elongation. As shown in Figure 2e, rotating the O−H bond costs 0.85 eV on Cu(111), and its elongation to reach the TS costs 0.75 eV. This is clearly distinct from H_2O and CH_3OH dissociation, where the energy cost of the O−H bond stretching dominates ΔE_{Act}. Compared with H_2O and CH_3OH, both having ΔE_{Ads} = −0.17 eV on Cu(111), *OH binds to the surface considerably stronger, with ΔE_{Ads} = −3.22 eV. According to valence shell electron pair repulsion theory,[60] the stronger *OH binding should generally lead to O−H bond

https://doi.org/10.1021/acscatal.1c03405
ACS Catal. 2022, 12, 1237−1246

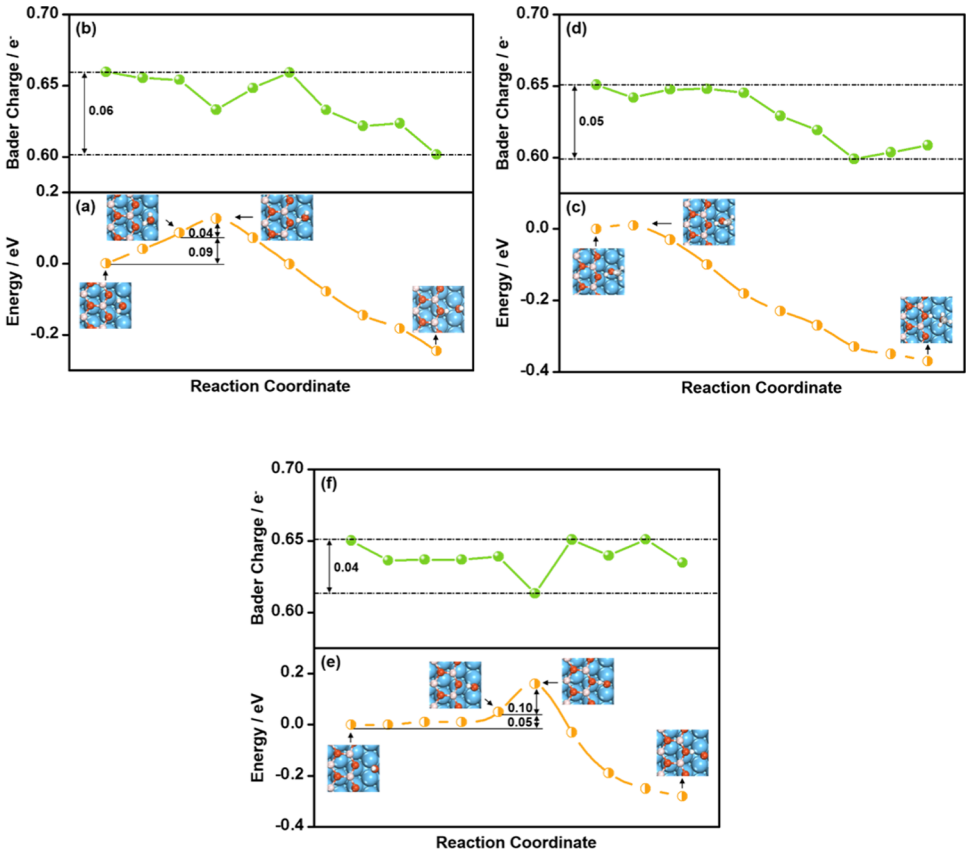

Figure 4. Energies and Bader charges on a Cu/ZnO interface of a dissociating H moiety along the reaction coordinate for $*H_2O \rightarrow *OH + *H$ (a, b); $*CH_3OH \rightarrow *CH_3O + *H$ (c, d); and $*OH + *O \rightarrow *O + *OH$ (e, f). Insets: snapshots of the initial, preconditioning, transition, and final states.

rotations with larger repulsion on the O−Cu bonds than in H_2O and CH_3OH. During O−H bond rotation, the Bader charge of the H moiety is only reduced by 0.16 e^- (Figure 2f). However, when the O−H bond is elongated and cleaved, the Bader charge of H is lowered by 0.43 e^-. H-like transfers are also observed on Co(0001) and Pt(111), whereas the O−H bond rotation on Pt(111) is considerably easier than on Cu(111) and Co(0001) by 0.65 and 0.38 eV (Figures S3 and S4). This is because *OH binds atop on Pt(111) with the O−H bond tilted toward the surface plane (Figure S4e), in contrast with the adsorption at hollow sites observed on Cu(111) and Co(0001), where the O−H bond is perpendicular to the surface plane. We note in passing that the ΔE_{Act} and TS structures calculated here (Table S6 and Figures 2, S3, and S4) agree well with previous DFT studies.[13,19,57−59]

3.2. H_2O, CH_3OH, and OH Activation on TiO_2(110) and $Ti_3C_2O_2$(0001). Compared to metal surfaces, the bridge O vacancy of TiO_2(110) (Figure 1b) binds H_2O and CH_3OH more strongly, with ΔE_{Ads} of −0.90 and −0.99 eV, respectively (Table S5). These results can be rationalized considering the more significant electron donation from the lone-pair electrons of O ($2p_z$) in H_2O and CH_3OH to the empty 3d states on TiO_2(110) vs 3d and 4s states on Cu(111). This is seen from the deep-lying orbital hybridization in the energy window between −9 and −3 eV in Figure S5a,b. We attribute this to Ti atoms at the bridge O vacancy of TiO_2(110) having more empty states than metallic Cu to accept lone-pair electrons.

Extracting H from the most stable states of adsorbed H_2O at the bridge O vacancy to yield two adjacent bridge OH moieties on TiO_2(110), has a reaction barrier of 0.34 eV (Table S6), in agreement with previous DFT studies.[61] As shown in Figures 3a and S2 and Table S4, the reaction coordinate begins with water rotating to form a hydrogen bond with a neighboring bridge O site. Similar to the case of metals, the O−H bond rotation of adsorbed H_2O only gives rise to a slight increase in energy (0.12 eV) and O−H bond length (0.02 Å); see Figure 3a and Table S1. After that, the O−H bond is elongated to 1.21 Å, and the TS is subsequently reached upon a small energy cost of 0.22 eV. This is noticeably different compared to metals, which have a substantial energy increase (0.85 eV on Cu(111) in Figure 2a) for the cleavage of the O−H bond in H_2O.

Figure 3b shows that the Bader charge of H varies by no more than 0.05 e^- in the range of 0.61−0.66 e^- when it moves from H_2O to O at the bridge site of TiO_2(110). In view of this, H_2O decomposition on TiO_2(110) is a proton-like transfer process, does not involve a significant variation of electron charges and has low dissociation barriers, unlike the H-like transfer processes on metals. Similar to H_2O dissociation, CH_3OH dissociation on TiO_2(110) is facile, with ΔE_{Act} = 0.44 eV (Table S6 and Figure 3c). Again, the low barrier is linked to a proton-like transfer during the dissociation process, wherein no significant change in the charge of the H moiety is noticed (Figure 3d).

*OH dissociation at the bridge O vacancy on TiO_2(110) has a considerably higher ΔE_{Act} (1.26 eV) than H_2O and CH_3OH dissociation; see Table S6 and Figure 3e. Since the charge of H only varies by 0.06 e^- along the reaction coordinate (Figure

https://doi.org/10.1021/acscatal.1c03405
ACS Catal. 2022, 12, 1237−1246

3f), the high ΔE_{Act} must stem from other reasons. The reaction coordinate proceeds through an initial O−H bond rotation to form a hydrogen bond with an adjacent bridge O site (Table S4), with a large associated energy cost of 0.62 eV (Figure 3e). This is in contrast with H_2O and CH_3OH dissociation, where the rotation only increases the energy by 0.12−0.27 eV. We also observed a more difficult rotation of *OH compared to H_2O and CH_3OH on metals, which we attribute to the stronger OH adsorption compared with H_2O and CH_3OH adsorption (−4.86 vs −0.90 and −0.99 eV), resulting in O−H bond rotations with larger repulsion. According to Table S6 and Figures S3e and S4e, OH dissociation on TiO_2(110) has a higher barrier than on Co(0001) and Pt(111) by 0.27−0.31 eV, indicating that TiO_2(110) is not efficient for OH activation despite its enhancement of H_2O and CH_3OH activation.

With respect to TiO_2(110), the binding energies of H_2O and CH_3OH on $Ti_3C_2O_2$(0001) are slightly weaker by no more than 0.10 eV, whereas the binding energies of dissociated species such as *OH and *CH_3O are considerably stronger by 0.34−0.46 eV; see Table S5. Accordingly, not only are H_2O and CH_3OH dissociations more exothermic on $Ti_3C_2O_2$(0001) than on TiO_2(110), but ΔE_{Act} also decreases by 0.21−0.30 eV on this MXene (Table S6 and Figure S6). However, the case is different for OH dissociation, which has ΔE_{Act} = 1.40 eV on $Ti_3C_2O_2$(0001), slightly higher than on TiO_2(110) by 0.14 eV. Again, the facile dissociation of H_2O and CH_3OH is linked to a proton-like transfer process, whereas strong OH adsorption (−5.20 eV) is responsible for the unfavorable dissociation activity on $Ti_3C_2O_2$(0001), as discussed above for TiO_2(110). Finally, we note that both TiO_2(110) and $Ti_3C_2O_2$(0001) bind OH at the bridge or hollow sites with rather negative adsorption energies, which leads to high dissociation barriers. However, oxides binding OH on top sites may display weaker adsorption energies and, thus, more facile O−H bond rotation and faster dissociation kinetics.

To close this section, we note that, in agreement with our observations, Chandler et al. found through a combination of kinetics experiments, infrared spectroscopy experiments, and DFT calculations that H-like and proton-like transfers lead to dissimilar activities for H_2 dissociation on TiO_2-supported Au catalysts. Specifically, the heterolytic H_2 dissociation, resulting in a formal hydride adsorbed on Au sites and a proton bound to the support to produce a TiOH group (proton-like transfer), has a lower barrier than the homolytic H_2 dissociation on Au sites (H-like transfer) by 0.46−0.57 eV.[62]

3.3. H_2O, CH_3OH, and OH Activation on Cu/ZnO and Pt/FeO Interfaces. We now turn our attention to metal/oxide interfaces, in particular Cu/ZnO and Pt/FeO. As shown in Figure 4, both H_2O and CH_3OH bind through O at the top sites of Cu atoms, with O−H bonds pointing to the O atom at the interface of Cu/ZnO ($\angle$O−H−O = 154 and 160°; d_{O-H} = 1.76 and 1.41 Å), leading to the formation of strong hydrogen bonds. Such bonds stabilize H_2O and CH_3OH by 0.50 and 0.37 eV compared to Cu(111) (Table S5). *CH_3O and *OH prefer to bind at the fcc site on the Cu terrace, with lower ΔE_{Ads} than on Cu(111) by ∼0.20 eV (Figures 4 and S7 and Table S5). OH is tilted toward the interfacial O atom on Cu/ZnO, in contrast to Cu(111), where the O−H bond is perpendicular to the surface plane. This implies that interfacial O atoms have an attractive interaction with H moieties in OH, which may facilitate the rotation of the O−H bond. H binds to the O atom at the interface between Cu(111) and ZnO (Figure S7), with a ΔE_{Ads} that is 0.63 eV more negative than on Cu(111). These adsorption properties result in more favorable thermochemistry for H_2O, OH, and CH_3OH dissociation on Cu/ZnO, with ΔH values from −0.24 to −0.37 eV (Table S6).

As shown in Figure 4, H_2O, OH, and CH_3OH dissociation on Cu/ZnO proceed through proton-like transfer processes, with a remarkably low ΔE_{Act} of 0.01−0.16 eV (Table S6). In particular, OH dissociation has ΔE_{Act} = 0.16 eV, which is substantially lower than those of metal and oxide surfaces (in the range of 0.95−1.60 eV, see Table S6). H_2O and CH_3OH form strong hydrogen bonds with interfacial O atoms upon adsorption at Cu/ZnO (Figure 4a,c), which avoid O−H bond rotation over wide angles (Figure S2 and Table S4) and their high associated energy costs. The rotation of the O−H bond in OH only costs 0.05 eV (Figure 4e), which is an order of magnitude lower than the corresponding values of 0.85, 0.62, and 0.68 eV on Cu(111), TiO_2(110), and $Ti_3C_2O_2$(0001). Compared to Cu(111), the inclination of OH toward an interfacial O atom at the IS and the formation of a hydrogen bond at the preconditioning state on the Cu/ZnO interface ease the rotation of O−H bonds. After the rotation, H−O−Cu bonds on the Cu/ZnO interface have an average angle of 104°, which is considerably larger than the 69° observed on Cu(111). Following valence shell electron pair repulsion theory,[60] this results in lesser repulsion between O−H and O−Cu bonds and lower associated energy costs on the interface. In addition, the moderate binding of OH on the Cu/ZnO interface (ΔE_{Ads} = −3.41 eV) is considerably weaker than on TiO_2(110) and $Ti_3C_2O_2$(0001) by 1.45 and 1.79 eV (Table S5), which facilitates O−H bond rotation.

Besides O−H bond rotation, the proton-like transfer during H_2O, OH, and CH_3OH dissociation on Cu/ZnO is also facile, with energy costs of 0.10 eV or less (Figure 4). The O−H−O bond angles fall in the range of 160−168° after the O−H bond rotation during H_2O, OH, and CH_3OH dissociation, which are closer to the linear configuration than those on TiO_2(110) and $Ti_3C_2O_2$(0001) (130−141°). Furthermore, the O−H bond distances on Cu/ZnO are 1.29−1.59 Å after O−H bond rotation, which are shorter than the corresponding values on TiO_2(110) and $Ti_3C_2O_2$(0001) (1.68−1.89 Å). Such favorable configurations lead to stronger hydrogen bonds and proton-like transfer of H moieties with a concomitant low ΔE_{Act} (Figure 4).

The Fe-terminated Pt/FeO interface has a strong oxygen affinity, evinced by its OH and CH_3O binding energies (Table S5). In fact, they are more negative than those of Pt(111) by 0.77 and 0.68 eV. However, atomic O binds at the Pt/FeO interface more weakly than on Pt(111) by 0.59 eV. This is because atomic O is only coordinated to an Fe atom at the interface, while three Pt atoms are available on Pt(111) (Figure S7Ca,Ga). In addition, H_2O, CH_3OH, and H at the interface have comparable ΔE_{Ads} to Pt(111). These results indicate that H_2O and CH_3OH dissociation are thermodynamically more favorable on Pt/FeO interfaces than on Pt(111) (Table S6), whereas the case is markedly different for OH dissociation.

As shown in Table S6 and Figure S8a−d, H_2O and CH_3OH dissociation proceed at the Pt/FeO interface through a proton-like transfer process with ΔE_{Act} values of 0.59 and 0.55 eV, which are lower than on Pt(111) (via a H-like transfer) by 0.33 and 0.32 eV, respectively. However, compared to other proton-like transfer processes on TiO_2(110), $Ti_3C_2O_2$(0001), and Cu/ZnO, the barriers are substantially higher. This may stem

https://doi.org/10.1021/acscatal.1c03405
ACS Catal. 2022, 12, 1237−1246

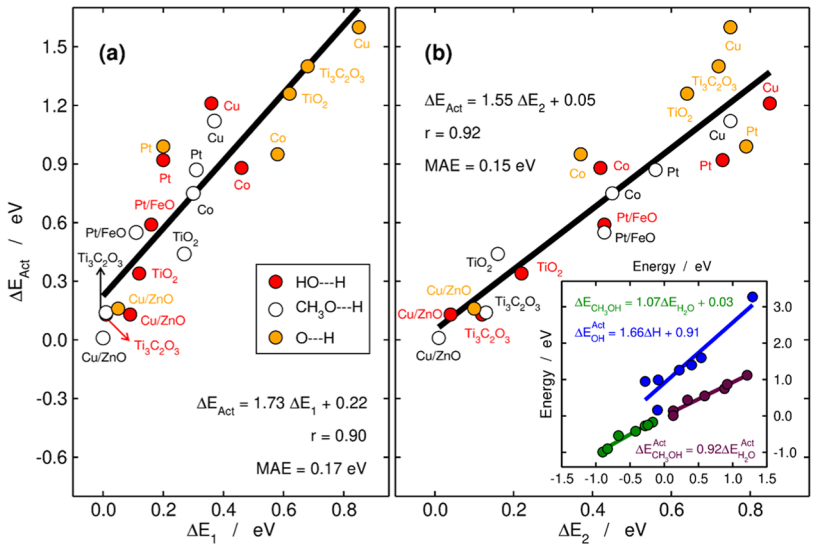

Figure 5. Trends in the kinetics and thermodynamics of H_2O (red), CH_3OH (white), and OH (orange) catalytic dissociation. (a) Overall activation energy (ΔE_{Act}) as a function of the preconditioning barrier (ΔE_1). (b) Overall activation energy as a function of the dissociation barrier (ΔE_2). The equations of the linear fits are provided in each case together with the correlation coefficients (r) and the associated mean absolute errors (MAEs). Inset: Brønsted–Evans–Polanyi (BEP) relationship for *OH scission (blue), correlations between the adsorption energies of H_2O and CH_3OH (green), and the activation energies of their scissions (maroon). The r values are 0.93, 0.98, and 0.98, and the MAEs are 0.27, 0.04, and 0.05 eV, respectively.

from the fact that after the O–H bond rotation, H_2O and CH_3OH binding at interfacial Fe sites cannot form hydrogen bonds as effectively as other oxides and metal/oxide interfaces, with O–H–O bond angles of 138 and 117° and O–H distances of 1.60 and 1.91 Å, respectively.

Unlike H_2O and CH_3OH dissociation, OH dissociation on Pt/FeO has a large barrier of 3.27 eV. Besides the unfavorable thermochemistry (ΔH = 1.29 eV), H-like transfers during OH dissociation at the Pt/FeO interface are observed from the IS to the TS and from there to the FS. According to Figure S8e,f, H binds to one Fe atom at the TS, with a variation in charge of 0.62 e^- with respect to the IS (H-like transfer). This differs from the proton-like transfer for H_2O and CH_3OH dissociation on Pt/FeO and can be understood from the adsorbate-interface structure. Each interfacial O binds to three Fe atoms and only one sp^3 hybridization orbital perpendicular to the surface is available to bind the dissociated H moieties. Compared to interfacial O, the O atoms in adsorbed H_2O and CH_3OH are higher by 0.75 and 1.28 Å, whereas that in OH is lower by 0.31 Å. This leads to a less effective overlap between O (adsorbate)–O (interface) orbitals in OH compared to H_2O and CH_3OH and, hence, unfavorable transfer of H moieties.

In Sections 3.2 and 3.3, we showed that hydrogen bonding plays an important role in O–H scission on oxides, MXenes, and metal/oxide interfaces. Its effect is twofold: (1) H_2O and CH_3OH first undergo an O–H bond rotation to form a hydrogen bond with a neighboring O at the preconditioning states of oxidized surfaces and interfaces. This often leads to an energy stabilization of 0.20–0.30 eV[63,64] and smaller energetic costs for O–H bond rotation. For instance, the preconditioning barriers ΔE_1 for H_2O/CH_3OH rotation on the oxidized surfaces and interfaces fall in the range of 0.01–0.16/0.00–0.27 eV, which are lower than those of metals (0.20–0.46/0.30–0.37 eV; see Table S7). (2) Hydrogen bonds facilitate proton-like transfers, which are less energy-demanding than the H-like transfers observed on metals. For example, the dissociation barriers ΔE_2 for H_2O and CH_3OH in Table S7 for oxidized surfaces and interfaces (0.01–0.43 eV) are appreciably lower than those of metals (0.42–0.85 eV).

Moreover, increasingly strong hydrogen bonding on oxidized surfaces and interfaces accelerates proton-like transfers. For instance, the Cu/ZnO interface with more linear O–H–O bond angles and shorter O–H distances (i.e., stronger hydrogen bonding) in the preconditioning steps for H_2O, CH_3OH, and OH scission has ΔE_2 = 0.04, 0.01, and 0.10 eV, lower than the corresponding values of the other oxidized surfaces and interfaces (0.12–0.43, 0.13–0.43. and 0.64–0.71 eV, respectively; see Table S7).

3.4. Systematic Trends in the Scission of O–H Bonds.

Beyond the case-by-case analysis in Figures 2–4, S3, S4, S6, and S8, it is possible to extract overall trends from the data in this study. ΔE_{Act} can be split into two parts, namely, a preconditioning barrier and a dissociation barrier (hereon denoted as ΔE_1 and ΔE_2, respectively; see Table S7; see also Sections 2 and S1 for the determination of preconditioning states). ΔE_1 is mostly related to the rotation of the O–H bonds, whereas ΔE_2 corresponds to their actual cleavage. Figure 5 shows that ΔE_{Act}, ΔE_1, and ΔE_2 are approximately correlated in a linear manner, implying that the costs of rotating and cleaving O–H bonds are adsorbate- and materials-specific yet proportional. All in all, lower ΔE_{Act} is consistently observed on oxidized materials and metal/oxide interfaces compared to metals. In addition, it is generally easier to cleave water and methanol than OH, except for Cu/ZnO interfaces, which cleave the three adsorbates with equally low barriers.

Furthermore, the inset in Figure 5b (blue line) shows that Brønsted–Evans–Polanyi (BEP) relations[65–67] hold for OH dissociation on the materials under study. These relations connect a thermodynamic variable (ΔH) easy to calculate using DFT with a kinetic variable (ΔE_{Act}) obtained through complicated transition-state searches. Although BEP relations are not observed for the activation of water and methanol, the

https://doi.org/10.1021/acscatal.1c03405
ACS Catal. 2022, 12, 1237–1246

inset in Figure 5 shows that their adsorption energies are proportional and so are the activation energies of their dissociation. Besides, Figures S9−S11 show that the adsorption energies of H_2O and CH_3OH, the total change in Bader charge (ΔBC) from the initial to the transition state, ΔBC^2, and the geometric mean of the Bader charges between the initial and transition states (denoted as $G(BC_{IS}, BC_{TS})$) are well correlated with ΔE_{Act}. In addition, since the Bader charges at the transition states might be difficult to assess, we found a correlation between the mean Bader charges of initial and transition states and the Bader charges of the final states, as shown in Figure S12. In sum, Figures 5 and S9−S12 suggest that, in spite of the wide diversity of the materials under study, there are energetic and electronic descriptors that might be used to devise high-throughput routines to search for efficient catalysts to cleave methanol, water, and/or OH. Interestingly, a good catalyst for H_2O activation is most certainly good for methanol activation, and vice versa. However, only in the presence of strong hydrogen bonding at interfaces might OH be inexpensively cleaved.

4. CONCLUSIONS

Knowledge of the underlying factors determining water and methanol activation is necessary for the design of enhanced catalysts for numerous reactions in catalysis. Finding such factors is usually complicated in view of the heterogeneity of the materials used to catalyze those processes and because of the great computational expenses associated with the assessment of kinetic barriers at surfaces and interfaces.

Here, through an interplay of CI-NEB transition-state searches and Bader charge analysis, we identified the key roles of proton-like transfer and O−H bond rotation in H_2O, OH, and CH_3OH activation on metals, oxides, MXenes, and metal/oxide interfaces. We provided a unifying framework for understanding the activation of O−H bonds, which allowed us to identify the active sites where it is more favorable, namely, at oxidized materials and metal/oxide interfaces, preferably offering strong hydrogen bonds. At those sites, O−H bond scission is accompanied by a proton-like transfer of H moieties and easy rotation of O−H bonds. Furthermore, we observed that an active material for cleaving water is likely suitable for methanol activation, but this need not be the case for OH dissociation.

The energetic proportionality between easy rotation and efficient O−H bond cleavage together with BEP and similar relations shown here might be used for the high-throughput in silico design of improved catalysts for reactions of industrial and technological interest in heterogeneous catalysis (e.g., methane/methanol steam reforming), electrochemistry (e.g., water splitting), and photocatalysis (e.g., methanol oxidation), where water, hydroxyl, and methanol are often present as reactants, intermediates, or products. In particular, the conspicuous differences between H_2O/CH_3OH and OH activation hint toward the use of carefully engineered multisite catalytic interfaces with controllable hydrogen bonding.

■ ASSOCIATED CONTENT

Supporting Information

The Supporting Information is available free of charge at https://pubs.acs.org/doi/10.1021/acscatal.1c03405.

Determination of preconditioning states; energetic and geometric data for adsorbates and elementary reactions; energies and Bader charges of dissociating H moieties along the reaction coordinates; projected density of states; correlation between activation energies, adsorption energies and Bader charges for H_2O and CH_3OH cleavage; and converged Cartesian coordinates and electronic energies (PDF)

■ AUTHOR INFORMATION

Corresponding Authors

Keju Sun − *Key Laboratory of Applied Chemistry, College of Environmental and Chemical Engineering, Yanshan University, Qinhuangdao 066004, China;* orcid.org/0000-0001-8791-4646; Email: kjsun@ysu.edu.cn

Federico Calle-Vallejo − *Department of Materials Science and Chemical Physics & Institute of Theoretical and Computational Chemistry (IQTCUB), University of Barcelona, 08028 Barcelona, Spain;* orcid.org/0000-0001-5147-8635; Email: f.calle.vallejo@ub.edu

Authors

Hai-Yan Su − *School of Chemical Engineering and Energy Technology, Dongguan University of Technology, Dongguan 523808, China;* orcid.org/0000-0001-9326-9647

Xiang-Kui Gu − *Department of Chemical Physics, College of Chemistry and Materials Science, Hefei National Laboratory for Physical Sciences at the Microscale, iChEM, CAS Center for Excellence in Nanoscience, University of Science and Technology of China, Hefei 230026, China;* orcid.org/0000-0001-6537-7026

Sha-Sha Wang − *Department of Chemical Physics, College of Chemistry and Materials Science, Hefei National Laboratory for Physical Sciences at the Microscale, iChEM, CAS Center for Excellence in Nanoscience, University of Science and Technology of China, Hefei 230026, China*

Jing Zhu − *Department of Chemical Physics, College of Chemistry and Materials Science, Hefei National Laboratory for Physical Sciences at the Microscale, iChEM, CAS Center for Excellence in Nanoscience, University of Science and Technology of China, Hefei 230026, China*

Wei-Xue Li − *Department of Chemical Physics, College of Chemistry and Materials Science, Hefei National Laboratory for Physical Sciences at the Microscale, iChEM, CAS Center for Excellence in Nanoscience, University of Science and Technology of China, Hefei 230026, China;* orcid.org/0000-0002-5043-3088

Chenghua Sun − *Centre for Translational Atomaterials, Swinburne University of Technology, Hawthorn, VIC 3122, Australia;* orcid.org/0000-0001-7654-669X

Complete contact information is available at: https://pubs.acs.org/10.1021/acscatal.1c03405

Notes

The authors declare no competing financial interest.

■ ACKNOWLEDGMENTS

This work was supported by the National Natural Science Foundation of China [21872136, 22172026, 91945302], the National Key R&D Program of China [2017YFA0204800, 2017YFB0602205, 2018YFA0208603], the Chinese Academy of Sciences (QYZDJ-SSW-SLH054), the Guangdong Innovation Research Team for Higher Education [2017KCXTD030], and the High-level Talents Project of Dongguan University of

https://doi.org/10.1021/acscatal.1c03405
ACS Catal. 2022, 12, 1237−1246

Technology [KCYKYQD2017017]. The grants RTI2018-095460-B-I00, RYC-2015-18996, and MDM-2017-0767 were funded by MCIN/AEI/10.13039/501100011033 and by the "European Union". This work was also partly supported by Generalitat de Catalunya via the grant 2017SGR13.

REFERENCES

(1) Rodriguez, J. A.; Liu, P.; Hrbek, J.; Evans, J.; Perez, M. Water Gas Shift Reaction on Cu and Au Nanoparticles Supported on $CeO_2(111)$ and $ZnO(000\bar{1})$: Intrinsic Activity and Importance of Support Interactions. *Angew. Chem., Int. Ed.* **2007**, *46*, 1329−1332.
(2) Yong, S. T.; Ooi, C. W.; Chai, S. P.; Wu, X. S. Review of Methanol Reforming-Cu-Based Catalysts, Surface Reaction Mechanisms, and Reaction Schemes. *Int. J. Hydrogen Energy* **2013**, *38*, 9541−9552.
(3) Jones, G.; Jakobsen, J. G.; Shim, S. S.; Kleis, J.; Andersson, M. P.; Rossmeisl, J.; Abild-Pedersen, F.; Bligaard, T.; Helveg, S.; Hinnemann, B.; Rostrup-Nielsen, J. R.; Chorkendorff, I.; Sehested, J.; Nørskov, J. K. First Principles Calculations and Experimental Insight into Methane Steam Reforming over Transition Metal Catalysts. *J. Catal.* **2008**, *259*, 147−160.
(4) Pitarch, J.; Ruiz-Lopez, M. F.; Silla, E.; Pascual-Ahuir, J.-L.; Tunon, I. Neutral and Alkaline Hydrolyses of Model β-Lactam Antibiotics. An ab Initio Study of Water Catalysis. *J. Am. Chem. Soc.* **1998**, *120*, 2146−2155.
(5) Bustamante, F.; Cordoba, F.; Yates, M.; de Correa, C. M. The Promotion of Cobalt Mordenite by Palladium for the Lean CH 4SCR of NO_x in Moist Streams. *Appl. Catal., A* **2002**, *234*, 127−136.
(6) Harris, R. H.; Boyd, V. J.; Hutchings, G. J.; Taylor, S. H. Water as a Promoter of the Complete Oxidation of Volatile Organic Compounds over Uranium Oxide Catalysts. *Catal. Lett.* **2002**, *78*, 369−372.
(7) Albanese, D.; Landini, D.; Maia, A.; Penso, M. Key Role of Water for Nucleophilic Substitutions in Phase-Transfer-Catalyzed Processes: A Mini-Review. *Ind. Eng. Chem. Res.* **2001**, *40*, 2396−2401.
(8) Dat, M.; Okumura, M.; Tsubota, S.; Haruta, M. Vital Role of Moisture in the Catalytic Activity of Supported Gold Nanoparticles. *Angew. Chem., Int. Ed.* **2004**, *43*, 2129−2132.
(9) Carrasco, J.; Hodgson, A.; Michaelides, A. A Molecular Perspective of Water at Metal Interfaces. *Nat. Mater.* **2012**, *11*, 667−674.
(10) Pourbaix, M. *Atlas of Electrochemical Equilibria in Aqueous Solutions*, 2nd English ed.; National Association of Corrosion Engineers: Houston, TX, 1974.
(11) Williams, K.; Burstein, T. Low Temperature Fuel Cells: Interactions between Catalysts and Engineering Design. *Catal. Today* **1997**, *38*, 401−410.
(12) Rossmeisl, J.; Ferrin, P.; Tritsaris, G. A.; Nilekar, A. U.; Koh, S.; Bae, S. E.; Brankovic, S. R.; Strassere, P.; Mavrikakis, M. Bifunctional Anode Catalysts for Direct Methanol Fuel Cells. *Energy Environ. Sci.* **2012**, *5*, 8335−8342.
(13) Greeley, J.; Mavrikakis, M. A First-Principles Study of Methanol Decomposition on Pt(111). *J. Am. Chem. Soc.* **2002**, *124*, 7193−7201.
(14) Kakati, N.; Maiti, J.; Lee, S. H.; Jee, S. H.; Viswanathan, B.; Yoon, Y. S. Anode Catalysts for Direct Methanol Fuel Cells in Acidic Media: Do We Have Any Alternative for Pt or Pt−Ru? *Chem. Rev.* **2014**, *114*, 12397−12429.
(15) Drew, K.; Girishkumar, G.; Vinodgopal, K.; Kamat, P. V. Boosting Fuel Cell Performance with A Semiconductor Photocatalyst: TiO_2/Pt-Ru Hybrid Catalyst for Methanol Oxidation. *J. Phys. Chem. B* **2005**, *109*, 11851−11857.
(16) Rodriguez, J. A.; Ma, S.; Liu, P.; Hrbek, J.; Evans, J.; Pérez, M. Activity of CeO_x and TiO_x Nanoparticles Grown on Au(111) in the Water-Gas Shift Reaction. *Science* **2007**, *318*, 1757−1760.
(17) Campbell, C. T.; Daube, K. A. A Surface Science Investigation of the Water-Gas Shift Reaction on Cu(111). *J. Catal.* **1987**, *104*, 109−119.
(18) Liu, P.; Rodriguez, J. A. Water-Gas-Shift Reaction on Metal Nanoparticles and Surfaces. *J. Chem. Phys.* **2007**, *126*, No. 164705.
(19) Gokhale, A. A.; Dumesic, J. A.; Mavrikakis, M. On the Mechanism of Low-Temperature Water Gas Shift Reaction on Copper. *J. Am. Chem. Soc.* **2008**, *130*, 1402−1414.
(20) Shekhar, M.; Wang, J.; Lee, W. S.; Williams, W. D.; Kim, S. M.; Stach, E. A.; Miller, J. T.; Delgass, W. N.; Ribeiro, F. H. Size and Support Effects for the Water-Gas Shift Catalysis over Gold Nanoparticles Supported on Model Al_2O_3 and TiO_2. *J. Am. Chem. Soc.* **2012**, *134*, 4700−4708.
(21) Mudiyanselage, K.; Senanayake, S. D.; Feria, L.; Kundu, S.; Baber, A. E.; Graciani, J.; Vidal, A. B.; Agnoli, S.; Evans, J.; Chang, R.; Axnanda, S.; Liu, Z.; Sanz, J. F.; Liu, P.; Rodriguez, J. A.; Stacchiola, D. J. Importance of the Metal−Oxide Interface in Catalysis: In Situ Studies of the Water−Gas Shift Reaction by Ambient-Pressure X-ray Photoelectron Spectroscopy. *Angew. Chem., Int. Ed.* **2013**, *52*, 5101−5105.
(22) Li, Y. Y.; Kottwitz, M.; Vincent, J. L.; Enright, M. J.; Liu, Z. Y.; Zhang, L. H.; Huang, J. H.; Senanayake, S. D.; Yang, W.-C.; Crozier, P. A.; Nuzzo, R. G.; Frenkel, A. I. Dynamic Structure of Active Sites in Ceria-Supported Pt Catalysts for the Water Gas Shift Reaction. *Nat. Commun.* **2021**, *12*, No. 914.
(23) Fu, X.-P.; Guo, L.-W.; Wang, W.-W.; Ma, C.; Jia, C.-J.; Wu, K.; Si, R.; Sun, L.-D.; Yan, C.-H. Direct Identification of Active Surface Species for Water-Gas Shift Reaction on Gold-Ceria Catalyst. *J. Am. Chem. Soc.* **2019**, *141*, 4613−4623.
(24) Zhu, M. H.; Tian, P. F.; Kurtz, R.; Lunkenbein, T.; Xu, J.; Schlögl, R.; Wachs, I. E.; Han, Y.-F. Strong Metal-Support Interactions between Copper and Iron Oxide during the High-Temperature Water-Gas Shift Reaction. *Angew. Chem., Int. Ed.* **2019**, *58*, 9083−9087.
(25) Xu, M.; Yao, S. Y.; Rao, D. M.; Niu, Y. M.; Liu, N.; Peng, M.; Zhai, P.; Man, Y.; Zheng, L.-R.; Wang, B.; Zhang, B. S.; Ma, D.; Wei, M. Insights into Interfacial Synergistic Catalysis over $Ni@TiO_{2-x}$ Catalyst toward Water-Gas Shift Reaction. *J. Am. Chem. Soc.* **2018**, *140*, 11241−11251.
(26) Sun, K. J.; Kohyama, M.; Tanaka, S.; Takeda, S. Reaction Mechanism of the Low-Temperature Water−Gas Shift Reaction on Au/TiO_2 Catalysts. *J. Phys. Chem. C* **2017**, *121*, 12178−12187.
(27) Clausen, B. S.; Steffensen, G.; Fabius, B.; Villadsen, J.; Feidenhansl, R.; Topsøe, H. In Situ Cell for Combined XRD and on-line Catalysis Tests: Studies of Cu-Based Water Gas Shift and Methanol Catalysts. *J. Catal.* **1991**, *132*, 524−535.
(28) Fu, Q.; Saltsburg, H.; Flytzani-Stephanopoulos, M. Active Nonmetallic Au and Pt Species on Ceria-Based Water-Gas Shift Catalysts. *Science* **2003**, *301*, 935−938.
(29) Liu, Z.-P.; Jenkins, S. J.; King, D. A. Origin and Activity of Oxidized Gold in Water-Gas-Shift Catalysis. *Phys. Rev. Lett.* **2005**, *94*, No. 196102.
(30) Peppley, B. A.; Amphlett, J. C.; Kearns, L. M.; Mann, R. F. Methanol-Steam Reforming on $Cu/ZnO/Al_2O_3$ Catalysts. Part 2. A Comprehensive Kinetic Model. *Appl. Catal., A* **1999**, *179*, 31−49.
(31) Grunwaldt, J. D.; Molenbroek, A. M.; Topsøe, N. Y.; Topsøe, H.; Clausen, B. S. In Situ Investigations of Structural Changes in Cu/ZnO Catalysts. *J. Catal.* **2000**, *194*, 452−460.
(32) Günter, M. M.; Ressler, T.; Jentoft, R. E.; Bems, B. Redox Behavior of Copper Oxide/Zinc Oxide Catalysts in the Steam Reforming of Methanol Studied by in Situ X-Ray Diffraction and Absorption Spectroscopy. *J. Catal.* **2001**, *203*, 133−149.
(33) Agrell, J.; Birgersson, H.; Boutonnet, M. Steam Reforming of Methanol over a $Cu/ZnO/Al_2O_3$ Catalyst: A Kinetic Analysis and Strategies for Suppression of CO Formation. *J. Power Sources* **2002**, *106*, 249−257.
(34) Hansen, P. L.; Wagner, J. B.; Helveg, S.; Rostrup-Nielsen, J. R.; Clausen, B. S.; Topsøe, H. Atom-Resolved Imaging of Dynamic Shape Changes in Supported Copper Nanocrystals. *Science* **2002**, *295*, 2053−2055.
(35) Rameshan, C.; Stadlmayr, W.; Penner, S.; Lorenz, H.; Memmel, N.; Havecker, M.; Blume, R.; Teschner, D.; Rocha, T.; Zemlyanov,

https://doi.org/10.1021/acscatal.1c03405
ACS Catal. 2022, 12, 1237−1246

D.; et al. Hydrogen Production by Methanol Steam Reforming on Copper Boosted by Zinc-Assisted Water Activation. *Angew. Chem., Int. Ed.* **2012**, *51*, 3002−3006.
(36) Henkelman, G.; Jonsson, H. Improved Tangent Estimate in the Nudged Elastic Band Method for Finding Minimum Energy Paths and Saddle Points. *J. Chem. Phys.* **2000**, *113*, 9978.
(37) Yu, M.; Trinkle, D. R. Accurate and Efficient Algorithm for Bader Charge Integration. *J. Chem. Phys.* **2011**, *134*, No. 064111.
(38) Kresse, G.; Furthmüller, J. Efficient Iterative Schemes for Ab Initio Total-Energy Calculations Using a Plane-wave Basis Set. *Phys. Rev. B* **1996**, *54*, 11169−11186.
(39) Blöchl, P. E. Projector Augmented-Wave Method. *Phys. Rev. B* **1994**, *50*, 17953−17979.
(40) Perdew, J. P.; Burke, K.; Ernzerhof, M. Generalized Gradient Approximation Made Simple. *Phys. Rev. Lett.* **1996**, *77*, 3865−3868.
(41) Grimme, S.; Ehrlich, S.; Goerigk, L. Effect of the Damping Function in Dispersion Corrected Density Functional Theory. *J. Comput. Chem.* **2011**, *32*, 1456−1465.
(42) Lide, D. R. *CRC Handbook of Chemistry and Physics*, 88th ed.; CRC Press: Boca Raton, FL, 2007.
(43) Mashtalir, O.; Naguib, M.; Mochalin, V. N.; Dall'Agnese, Y.; Heon, M.; Barsoum, M. W.; Gogotsi, Y. Intercalation and Delamination of Layered Carbides and Carbonitrides. *Nat. Commun.* **2013**, *4*, No. 1716.
(44) Monkhorst, H. J.; Pack, J. D. Special Points for Brillouin-Zone Integrations. *Phys. Rev. B* **1976**, *13*, 5188−5192.
(45) Janotti, A.; Van de Walle, C. G. Native Point Defects in ZnO. *Phys. Rev. B* **2007**, *76*, No. 165202.
(46) Giordano, L.; Pacchioni, G.; Goniakowski, J.; Nilius, N.; Rienks, E. D. L.; Freund, H. J. Interplay between Structural, Magnetic, and Electronic Properties in a FeO/Pt(111) Ultrathin Film. *Phys. Rev. B* **2007**, *76*, No. 075416.
(47) Wang, S. S.; Su, H. Y.; Gu, X. K.; Li, W. X. Differentiating Intrinsic Reactivity of Copper, Copper−Zinc Alloy, and Copper/Zinc Oxide Interface for Methanol Steam Reforming by First-Principles Theory. *J. Phys. Chem. C* **2017**, *121*, 21553−21559.
(48) Fu, Q.; Li, W. X.; Yao, Y. X.; Liu, H. Y.; Su, H. Y.; Ma, D.; Gu, X. K.; Chen, L. M.; Wang, Z.; Zhang, H.; Wang, B.; Bao, X. H. Interface-Confined Ferrous Centers for Catalytic Oxidation. *Science* **2010**, *328*, 1141−1144.
(49) Su, H. Y.; Ma, X. F.; Sun, K. J.; Sun, C. H.; Xu, Y. J.; Calle-Vallejo, F. Trends in C−O and N−O Bond Scission on Rutile Oxides Described Using Oxygen Vacancy Formation Energies. *Chem. Sci.* **2020**, *11*, 4119−4124.
(50) Christensen, R.; Hansena, H. A.; Vegge, T. Identifying Systematic DFT Errors in Catalytic Reactions. *Catal. Sci. Technol.* **2015**, *5*, 4946−4949.
(51) Granda-Marulanda, L. P.; Rendón-Calle, A.; Builes, S.; Illas, F.; Koper, M. T. M.; Calle-Vallejo, F. A Semiempirical Method to Detect and Correct DFT-Based Gas-Phase Errors and Its Application in Electrocatalysis. *ACS Catal.* **2020**, *10*, 6900−6907.
(52) Kumagai, T.; Shiotari, A.; Okuyama, H.; Hatta, S.; Aruga, T.; Hamada, I.; et al. H-Atom Relay Reactions in Real Space. *Nat. Mater.* **2012**, *11*, 167−172.
(53) Kumagai, T.; Kaizu, M.; Okuyama, H.; Hatta, S.; Aruga, T.; Hamada, I.; Morikawa, Y. Tunneling Dynamics of A Hydroxyl Group Adsorbed on Cu(110). *Phys. Rev. B* **2009**, *79*, No. 035423.
(54) Meng, S.; Wang, E. G.; Gao, S. W. Water Adsorption on Metal Surfaces: A General Picture from Density Functional Theory Studies. *Phys. Rev. B* **2004**, *69*, No. 195404.
(55) Kolb, M. J.; Calle-Vallejo, F.; Juurlink, L. B. F.; Koper, M. T. M. Density Functional Theory Study of Adsorption of H_2O, H, O, and OH on Stepped Platinum Surfaces. *J. Chem. Phys.* **2014**, *140*, No. 134708.
(56) Schiros, T.; Takahashi, O.; Andersson, K. J.; Ostrm, H.; Pettersson, L. G. M.; Nilsson, A.; Ogasawara, H. The Role of Substrate Electrons in the Wetting of A Metal Surface. *J. Chem. Phys.* **2010**, *132*, No. 094701.
(57) Yang, Y. X.; White, M. G.; Liu, P. Theoretical Study of Methanol Synthesis from CO_2 Hydrogenation on Metal-Doped Cu(111) Surfaces. *J. Phys. Chem. C* **2012**, *116*, 248−256.
(58) Luo, W. J.; Asthagiri, A. Density Functional Theory Study of Methanol Steam Reforming on Co(0001) and Co(111) Surfaces. *J. Phys. Chem. C* **2014**, *118*, 15274−15285.
(59) Michaelides, A.; Hu, P. Catalytic Water Formation on Platinum: A First-Principles Study. *J. Am. Chem. Soc.* **2001**, *123*, 4235−4242.
(60) Gillespie, R. J. The VSEPR Model Revisited. *Chem. Soc. Rev.* **1992**, *21*, 59−69.
(61) Wendt, S.; Matthiesen, J.; Schaub, R.; Vestergaard, E. K.; Lægsgaard, E.; Besenbacher, F.; Hammer, B. Formation and Splitting of Paired Hydroxyl Groups on Reduced TiO_2(110). *Phys. Rev. Lett.* **2006**, *96*, No. 066107.
(62) Whittaker, T.; Kumar, K. B. S.; Peterson, C.; Pollock, M. N.; Grabow, L. C.; Chandler, B. D. H_2 Oxidation over Supported Au Nanoparticle Catalysts: Evidence for Heterolytic H_2 Activation at the Metal-Support Interface. *J. Am. Chem. Soc.* **2018**, *140*, 16469−16487.
(63) Su, H. Y.; Yang, M. M.; Bao, X. H.; Li, W. X. The Effect of Water on the CO Oxidation on Ag(111) and Au(111) Surfaces: A First-Principle Study. *J. Phys. Chem. C* **2008**, *112*, 17303−17310.
(64) Rendón-Calle, A.; Builes, S.; Calle-Vallejo, F. Substantial Improvement of Electrocatalytic Predictions by Systematic Assessment of Solvent Effects on Adsorption Energies. *Appl. Catal., B* **2020**, *276*, No. 119147.
(65) Wang, S.; Temel, B.; Shen, J.; Jones, G.; Grabow, L. C.; Studt, F.; Bligaard, T.; Abild-Pedersen, F.; Christensen, C. H.; Nørskov, J. K. Universal Brønsted-Evans-Polanyi Relations for C−C, C−O, C−N, N−O, N−N, and O−O Dissociation Reactions. *Catal. Lett.* **2011**, *141*, 370−373.
(66) Wang, S.; Petzold, V.; Tripkovic, V.; Kleis, J.; Howalt, J. G.; Skúlason, E.; Fernández, E. M.; Hvolbæk, B.; Jones, G.; Toftelund, A.; Falsig, H.; Björketun, M.; Studt, F.; Abild-Pedersen, F.; Rossmeisl, J.; Nørskov, J. K.; Bligaard, T. Universal Transition State Scaling Relations for (De)Hydrogenation over Transition Metals. *Phys. Chem. Chem. Phys.* **2011**, *13*, 20760−20765.
(67) Vojvodic, A.; Calle-Vallejo, F.; Guo, W.; Wang, S.; Toftelund, A.; Studt, F.; Martinez, J. I.; Shen, J.; Man, I. C.; Rossmeisl, J.; Bligaard, T.; Nørskov, J. K.; Abild-Pedersen, F. On the Behavior of Brønsted-Evans-Polanyi Relations for Rransition Metal Oxides. *J. Chem. Phys.* **2011**, *134*, No. 244509.

https://doi.org/10.1021/acscatal.1c03405
ACS Catal. 2022, 12, 1237−1246